Ultrasound Current Source Density Imaging of the Cardiac Activation Wave Using a Clinical Cardiac Catheter

Yexian Qin, Qian Li, Pier Ingram, Christy Barber, Zhonglin Liu, and Russell S. Witte*, *Member, IEEE*

***Abstract*—Ultrasound current source density imaging (UCSDI), based on the acoustoelectric (AE) effect, is a noninvasive method for mapping electrical current in 4-D (space + time). This technique potentially overcomes limitations with conventional electrical mapping procedures typically used during treatment of sustained arrhythmias. However, the weak AE signal associated with the electrocardiogram is a major challenge for advancing this technology. In this study, we examined the effects of the electrode configuration and ultrasound frequency on the magnitude of the AE signal and quality of UCSDI using a rabbit Langendorff heart preparation. The AE signal was much stronger at 0.5 MHz (2.99 μV/MPa) than 1.0 MHz (0.42 μV/MPa). Also, a clinical lasso catheter placed on the epicardium exhibited excellent sensitivity without penetrating the tissue. We also present, for the first time, 3-D cardiac activation maps of the live rabbit heart using only one pair of recording electrodes. Activation maps were used to calculate the cardiac conduction velocity for atrial (1.31 m/s) and apical (0.67 m/s) pacing. This study demonstrated that UCSDI is potentially capable of real-time 3-D cardiac activation wave mapping, which would greatly facilitate ablation procedures for treatment of arrhythmias.**

***Index Terms*—Acoustoelectric, cardiac activation, cardiac arrhythmia, cardiac mapping, electrocardiogram (ECG/EKG).**

I. Background and Theory

SUSTAINED cardiac arrhythmias, such as atrial fibrillation, affect more than four million Americans each year. In their most serious form, arrhythmias can be debilitating, life threatening, and require aggressive treatment. Radio frequency (RF) ablation remains the primary choice for treatment for drug-resistant arrhythmia with approximately 100,000 procedures performed annually in the U.S. [1]. Cryoablation has also been used in place of RF cauterization without improvement in the outcome to therapy [2].

Manuscript received May 17, 2014; revised July 21, 2014; accepted July 26, 2014. Date of publication August 7, 2014; date of current version December 18, 2014. *Asterisk indicates corresponding author.*

Y. Qin, P. Ingram, C. Barber, and Z. Liu are with the Department of Medical Imaging, University of Arizona, Tucson, AZ 85724 USA (e-mail: yexian@gmail.com; pier.ingram@gmail.com; cbarber@email.arizona.edu; zliu@email.arizona.edu).

Q. Li is with the College of Optical Sciences, University of Arizona, Tucson, AZ 85721 USA (e-mail: qli@optics.arizona.edu).

*R. S. Witte is with the Department of Medical Imaging, University of Arizona, Tucson, AZ 85724 USA and also with the College of Optical Sciences, University of Arizona, Tucson, AZ, USA (e-mail: rwitte@email.arizona.edu).

This paper contains supplemental material available online at http://ieeexplore.ieee.org (File size: 8 MB).

Color versions of one or more of the figures in this paper are available online at http://ieeexplore.ieee.org.

Digital Object Identifier 10.1109/TBME.2014.2345771

Catheter ablation involves electroanatomical mapping (EAM), which exploits magnetic or electric sensors to track the position of the catheter inside the heart. As the catheter is steered through the chambers with the aid of fluoroscopy, electrophysiological (EP) maps of the heart are produced. This procedure typically lasts for several hours before a complete map is generated, and the target region for ablation is identified. Because the EP map is generated over many cardiac cycles, the anatomical registration is often inaccurate, leading to a variety of artifacts and errors [3], [4]. One problem relates to the use of fluoroscopy, which uses ionizing radiation. Because fluoroscopy is inherently a 2-D modality, this can lead to registration errors. Misalignment between the cardiac anatomy and the EP mapping often results in multiple ablation regions until the arrhythmia is successfully arrested. It is clear, despite the technological achievements, there is considerable room for improving the process by reducing the number of erroneous ablations, accelerating the mapping procedure, and possibly targeting those who suffer from nonsustained arrhythmias, like ventricular tachycardia, which are currently untreatable with existing mapping and ablation methods.

In an effort to overcome limitations with existing EP mapping, this study examines ultrasound current source density imaging (UCSDI) as a tool that potentially facilitates and enhances mapping biopotentials in the heart. UCSDI is based on the acoustoelectric (AE) effect [5], an interaction between pressure and resistivity, which can be described as

$$\frac{\Delta\rho}{\rho_0} = -K\Delta P \tag{1}$$

where $\Delta\rho$ is the resistivity change of the tissue, ρ_0 is the direct current resistivity, ΔP is the ultrasonic pressure, and K is the AE interaction constant. Equation (1) indicates that a change in local pressure induces a modulation of resistivity with the conversion efficiency determined by K, which is approximately 0.04%/MPa in rabbit cardiac tissue [6]. The AE effect was first reported by Fox [7] and others have used it to study electrolytes in solution [8]–[11]. In recent years, interest has shifted to biomedical applications, including cancer detection [12], neural imaging [5], and cardiac mapping [13]. We also demonstrated detection and imaging of cardiac current in the live rabbit heart using intramuscular and intracardiac electrodes [14], [15].

For UCSDI, the AE effect modulates a tissue's resistivity near the focal region of the ultrasound beam. When current passes through tissue, the local change in resistivity induces a current modulation, detectable as a voltage across two electrodes. Based

on (1), the AE signal at different positions can be described as [13]

$$V_i^{\mathrm{AE}}(x_1, y_1, t) = -KP_0 \iiint (\vec{J}_i^{L} \cdot \vec{J}^{I})\rho_0 \, b(x - x_1, y - y_1, z) a(t - \frac{z}{c}) dx dy dz \quad (2)$$

where V_i^{AE} is the AE signal detected by recording lead i with lead field $\vec{J}_i^{L} = \vec{J}_i^{L}(x, y, z)$, distributed current source $\vec{J}^{I} = \vec{J}^{I}(x, y, z)$, electric resistivity $\rho_0 = \rho_0(x, y, z)$, ultrasound beam pattern $b(x, y, z)$, pressure pulse amplitude P_0, and ultrasound pulse waveform $a(t)$ (see [13] for the full derivation). A volume image proportional to the local current density distribution is generated as the ultrasound beam is swept across the sample. Note that according to (2), the size of the ultrasound focus and, therefore, the integration volume for UCSDI is highly dependent on the ultrasound wavelength [15].

There are several advantages of UCSDI compared to conventional electrical mapping. First, the detected electrical signal is confined to the focal region of the ultrasound beam. The spatial resolution is, therefore, similar to the dimensions of the ultrasound focal spot, typically on the order of a millimeter. Second, it is also possible to generate volume images of a time-varying current field using as few as one single electrode with a distant reference [16]. Another important advantage of UCSDI is that it can be readily combined, in real time, with pulse echo ultrasound to produce electrical maps coregistered with cardiac anatomy and motion.

One potential drawback of UCSDI for EAM is that the technique requires detecting a small signal close to background noise. However, according to (2), both the ultrasound and electrode parameters affect the sensitivity and spatial resolution of UCSDI. Consequently, this study will further examine the effects of the ultrasound frequency and electrode recording configuration on the AE signal using a live rabbit heart preparation. We will also demonstrate for the first time 2-D and 3-D mapping of the cardiac activation wave using a pair of recording electrodes on a clinical lasso catheter placed on the epicardium. These are important steps toward optimizing UCSDI and translating this technology to patients for fast EP mapping during ablation treatment for arrhythmias.

II. Instruments and Methods

A. Langendorff Isolated Rabbit Heart

All procedures were in accordance with the Institutional Animal Care and Use Committee at the University of Arizona. This study describes results from five adult New Zealand white rabbits, which were anaesthetized (ketamine and xylazine) and heparinized. Immediately following euthanasia (Beuthanasia-D), the hearts were quickly excised, cannulated, and mounted to a Langendorff perfusion system (Radnoti 120103EZ) with a flow controlled retroperfusion of Kreb–Henseleit (K-H) buffer, as shown in Fig. 1. The K-H buffer (NaCl, 117 mM; KCl, 4 mM; $MgSO_4$, 1.2 mM; KH_2PO_4, 1.1 mM; glucose, 5 mM; $NaHCO_3$, 25 mM; and $CaCl_2$, 2.6 mM) was placed in a reservoir, oxygenated with a mixture of 95% O_2 and 5% CO_2, pH balanced

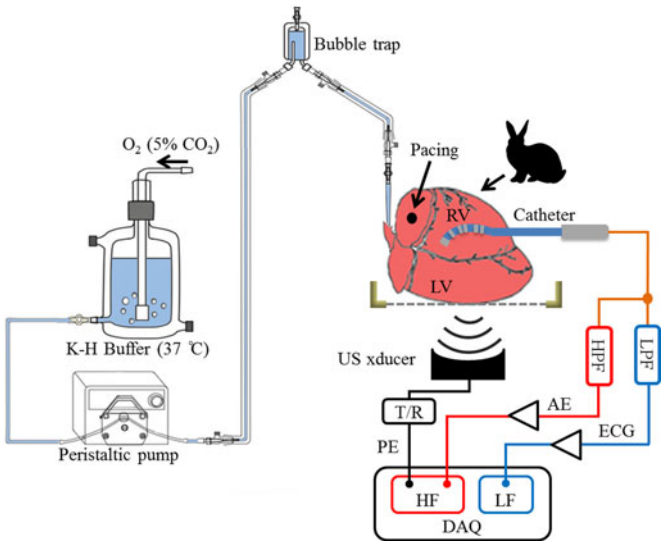

Fig. 1. Langendorff setup for UCSDI of the live rabbit heart and schematic diagram of the data acquisition (DAQ) system. The heart was perfused with 37 °C K-H buffer by Radnoti 120103EZ perfusion system. The ultrasound transducer (US xducer) was immersed in the 38 °C water tank underneath the heart and driven by a pulse/receiver (T/R). Recording electrodes were placed in or on the heart to detect both high frequency AE signals and low frequency (LF) electrocardiography (ECG) signals. HPF and LPF are the high- and low-pass filters for separating the AE and ECG signals. The high-frequency AE signal and pulse echo (PE) were recorded by an NI high-speed digitizer (HF); the standard LF ECG was recorded by a multifunction DAQ card.

to 7.44 and maintained at 37 °C. 2,3-Butanedione monoxime (BDM), an electromechanical decoupler, was optionally added to the buffer solution to limit motion of the heart while preserving electrical conduction. The buffer solution was driven by a peristaltic pump (Masterflex L/S, 7518-60, Cole Palmer) from the reservoir through a bubble trap to the cannulated heart.

B. Experimental Setup

The experimental setup is shown on the right side of Fig. 1. The cannulated heart was placed inside a custom plastic chamber with the left ventricle (LV) facing down on top of a thin acoustic window made of Mylar. The chamber was coupled to a large water tank that contained a focused ultrasound transducer. The tank was maintained at 38 °C to provide a physiologic environment for the heart.

The heart was paced with a pair of platinum needle electrodes (Grass Technologies) either at the right atrium (RA) or LV. The pacing signal was a 1-V rectangular pulse with a duration of 1 ms emitted by a function generator (Agilent 33220A). The pacing rate was set slightly above the intrinsic rate, typically 2.5–4 Hz.

Three electrical recording schemes were employed to detect signals from the right ventricle (RV): 1) two intramuscular tungsten needle electrodes inserted into the myocardium parallel to the long axis of the heart; 2) a pair of platinum disk electrodes (diameter = 2 mm) on a custom 18 element epicardial grid array (Ad-Tech Medical Instrument Corp.) placed on the epicardium; and 3) a pair of stainless steel electrodes on a 7F clinical cardiac catheter (Bioscience Webster Lasso) placed on the epicardium.

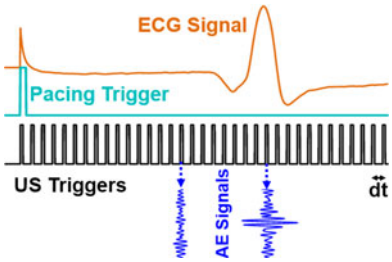

Fig. 2. Timing diagram of heart pacing, ultrasound pulsing, ECG recording, and AE signal acquisition. The heart was paced at 3 Hz or above its intrinsic rate. Each US trigger caused the waveform generator to produce a chirp excitation to the ultrasound transducer. The repetition rate of the ultrasound triggers (2 kHz) determined the sampling rate of the cardiac activation sequence. The low frequency-ECG was recorded simultaneously on the same electrodes.

The electrodes detected both the AE signal and the low frequency ECG signal (separable by high- and low-pass filters, as displayed in Fig. 1, right).

Two single-element focused ultrasound transducers were used for the experiments, including one with a center frequency of 0.5 MHz (Olympus Panametrics-NDT V389, $f = 54.6$ mm, dia $= 38$ mm) and the other at 1.0 MHz (Olympus Panametrics-NDT A392S, $f = 63.5$ mm, dia $= 38$ mm). The transducer was attached to a programmable stepper motor (Velmex Inc.), which controlled the position of the ultrasound beam.

C. Data Acquisition

As illustrated in Fig. 1, the AE and ECG signals were detected simultaneously and separated by high- and low-pass filters. One branch went through the high-pass filter (cutoff frequency $= 100$ kHz for the 0.5-MHz transducer, and 470 kHz for the 1-MHz transducer), preserving the AE signals modulated by the ultrasound beam. The AE signal was then differentially amplified (LeCroy DA 1855A) by 20 dB and collected on a digitizer card (National Instruments PXI 5105, sampling rate $= 10$ MHz, "HF" in Fig. 1) with another 40-dB gain. The other branch went through a low-pass filter (cutoff frequency $= 100$ kHz), preserving only the ECG signal, which was then amplified by 20 dB and collected on a multifunctional DAQ card (National Instruments PXI 6289, sampling rate $= 20$ kHz, "LF" in Fig. 1).

The experimental timing was also controlled by the multifunctional DAQ card, which generated two triggers: 1) the pacing trigger to the function generator (Agilent 33220A) for stimulating the heart, and 2) a 2-kHz burst trigger to another function generator (Keithley 3390), which sent out a frequency-encoded excitation signal (chirp) for pulsing the ultrasound transducer. Chirp excitation has been shown to be superior to short pulse excitation for detecting the AE signal [15]. The chirp signals used for this study had 20-μs duration, 1.0-MHz center frequency, and 0.54-MHz bandwidth for the 1-MHz transducer and 0.5-MHz center frequency and 0.27-MHz bandwidth for the 0.5-MHz transducer. The first ultrasound trigger for each cardiac cycle coincided with the pacing trigger, as shown in Fig. 2.

At each ultrasound trigger, the digitizer card (PXI 5105) acquired an RF trace (i.e., the AE signal), as displayed at the bottom of Fig. 2. The AE signal is typically strongest during the R-wave of the cardiac cycle. Meanwhile, a pulse receiver (Olympus 5077PR) captured the pulse echo signals, which were simultaneously acquired with the HF acquisition system.

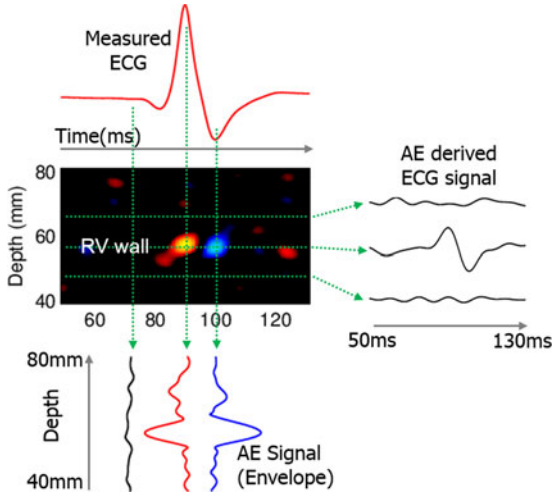

Fig. 3. Color M-mode UCSDI and ECG signal reconstruction. (top-left) measured low frequency ECG signal ($\mathrm{ECG_{LF}}$);(middle-left) color M-mode UCSDI image formed from the baseband AE signal, the horizontal axis represents slow time in millisecond (ms) starting from the pacing signal; the vertical axis represents the depth in millimeter (mm) from the ultrasound transducer element; (bottom-left) Envelope of the AE signals at three different time points (72, 90, and 100 ms); (right) $\mathrm{ECG_{AE}}$ at three different depths (48, 57, 66 mm) denoted by the horizontal green dashed lines in the color M-mode image. The depth values refer to the position relative to the ultrasound transducer at the origin.

The AE signals presented in Fig. 2 correspond to different time points during the cardiac cycle at a single location of the ultrasound transducer. Each of these traces is called an A-line. An M-mode image comprises a sequence of A-lines acquired at consecutive time points during the cardiac cycle (see Fig. 3). B-mode images comprise a collection of A-lines acquired along a line perpendicular to the ultrasound beam. Volume UCSDI is formed by collecting A-lines at different positions in the heart.

D. Signal Processing

To preserve the spatial resolution from ultrasound frequency coded excitation, a pulse compression algorithm was applied to both the AE and PE signals [15]. Each A-line was then filtered by a band-pass filter to reduce noise.The pass band was 0.3–0.8 MHz for the 0.5-MHz transducer and 0.5–1.2 MHz for the 1-MHz transducer. A band-pass filter (10–85 Hz) was further applied to the M-mode data matrix along the physiologic-time axis. Finally, each AE signal was demodulated and low-pass filtered to obtain the baseband signal. This produced a color M-mode with color and intensity indicating the direction and strength of the current density field, as shown in Fig. 3 (middle left). The vertical traces (see Fig. 3, bottom left) of the M-mode image represent the baseband AE signals at corresponding time points during the cardiac cycle, while the horizontal traces (see Fig. 3, right) represent the AE derived ECG signals ($\mathrm{ECG_{AE}}$) at different depths in the path of the ultrasound pulse. The same filter was also applied to the conventional ECG (see Fig. 3, top left) so that it could be compared directly to the $\mathrm{ECG_{AE}}$ signals.

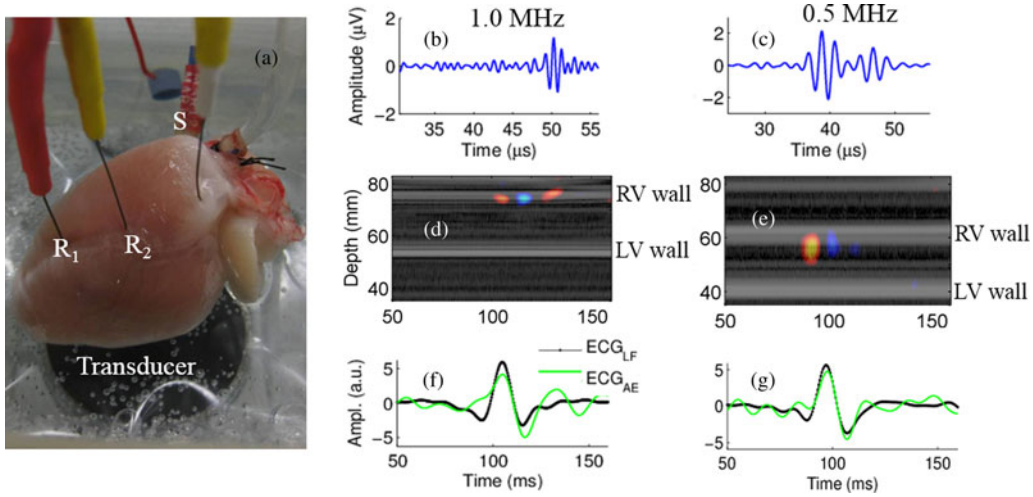

Fig. 4. Intramuscular UCSDI of live rabbit hearts using two different focused ultrasound transducers (1.0 and 0.5 MHz) and tungsten needle electrodes. (a) Rabbit heart in Langendorff chamber with two recording electrodes (R_1 and R_2) and a pair of pacing electrodes (S), which paced the heart at the RA at 3 Hz. The ultrasound transducer was located below the heart and focused at the RV wall; (b) and (c) filtered AE signals at the ECG_{LF} peak times of 105 and 92 ms, respectively; (d) and (e) overlay of the M-mode UCSDI (color) and PE (gray) images; (f) and (g) describe the ECG_{AE} signals (green) at the depth of 74 and 57 mm, respectively, with the ECG_{LF} (black) as a reference. The two columns describe data collected at two different ultrasound frequencies.

Activation times were determined from the delay between the pacing pulse and the peak of the ECG envelope.

III. Results

The effect of the electrode configuration and ultrasound frequency on the AE signal and UCSDI are investigated in the next two sections using the custom Langendorff setup for mapping the live rabbit heart.

A. UCSDI: Intramuscular Recording

Fig. 4 presents UCSDI results at two different ultrasound frequencies using needle recording electrodes. The same procedure was followed for two rabbit hearts, except that one was imaged with the 1.0-MHz transducer (3.4 MPa peak pressure) and the other at 0.5 MHz (0.7 MPa peak pressure). The geometric positions of the heart, recording and pacing electrodes, and the ultrasound transducer are illustrated in Fig. 4(a). For the 1.0- and 0.5-MHz transducers, the amplitudes of the filtered AE signals were 1.4 and 2.1 μV, respectively [see Fig. 4(b) and (c)]. After normalizing for pressure, the AE amplitude detected by the 0.5-MHz transducer was 3.0 μV/MPa. However, for the 1-MHz transducer, the AE amplitude was 0.41 μV/MPa, approximately seven times smaller than that of the 0.5-MHz transducer. It is also clear in the color M-mode UCSDI images [see Fig. 4(d) and (e)] that the 1-MHz transducer demonstrated better spatial resolution than the 0.5-MHz transducer. The full width at half maximum along the depth direction (ultrasound axial direction) was 3.19 and 6.21 mm, respectively, reflecting both the spatial resolution and dimensions of the current source through the wall of the RV. The tradeoff between sensitivity and resolution is consistent with our earlier phantom and simulation work [15]. The M-mode pulse echo images [gray in Fig 4(d) and (e)] also indicate the location of the LV and RV walls. Since the two transducers have different focal lengths, the pulse echo signal from the LV and RV walls occurred at different depths. The superimposed UCSDI and pulse echo images indicate that the source of the measured cardiac current is at the RV wall. A horizontal line at the maximum AE amplitude denotes the ECG_{AE} signal. This was compared with the simultaneously measured low frequency ECG_{LF} signal, as depicted in Fig. 4(f) and (g). The ECG_{AE} signals from UCSDI are consistent with the ECG_{LF}, although the location of the source of the two signals are different (i.e., UCSDI depends on the location of the US beam).

B. UCSDI: Epicardial Recording

We next evaluated UCSDI for epicardial recording using a planar array of disc electrodes, and also, a clinical cardiac catheter containing stainless steel electrodes.

For the electrode grid recording, two disc electrodes near the apex were selected to record the AE and ECG_{LF} signals. The peak AE signal with this configuration was 0.52 μV or 0.74 μV/MPa or approximately 25% of that measured with intramuscular electrodes.

Next, the clinical catheter was placed on the epicardium and exhibited much better sensitivity than the disc electrodes. Fig. 5 depicts the rabbit heart and the catheter position, as well as an M-mode image and sample ECG signals. The peak AE amplitude was 1.7 μV or 2.4 μV/MPa, which is comparable to using the intramuscular electrodes. This experiment included pacing at either the RA or apical region. The results depicted in Fig. 5 were produced with RA pacing and the ultrasound transducer at a fixed location. The ECG_{AE} and ECG_{LF} signals [see Fig. 5(c)] in this example were acquired simultaneously. This is consistent with the location of the ultrasound focal spot near recording electrode R_2.

The effect of the ultrasound frequency on the AE signal was further examined in the same heart using epicardial recording from the catheter. Scans were performed at 0.5 and 1 MHz

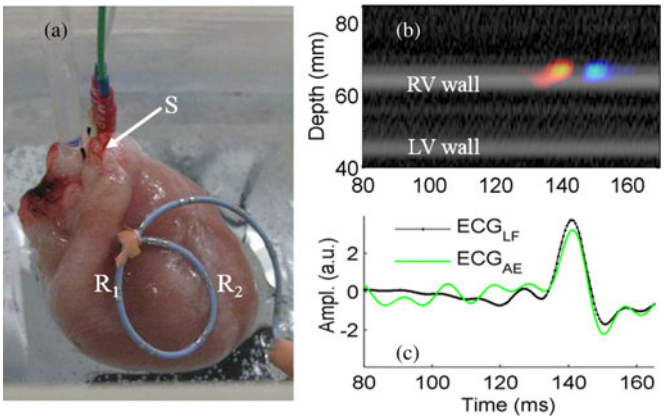

Fig. 5. Epicardial UCSDI of the live rabbit heart using the 0.5-MHz transducer and the lasso cardiac catheter. (a) Rabbit heart with catheter and recording electrodes R_1 and R_2. (b) M-mode pulse echo image (gray) superimposed on a color M-mode UCSDI. (c) ECG_{LF} (black) and ECG_{AE} (green) signals during cardiac cycle. The ECG_{AE} signal is taken at the RV wall at the depth of 66.7 mm relative to the transducer origin.

TABLE I
SUMMARY OF ULTRASOUND PARAMETERS AND SENSITIVITY FOR DETECTING THE AE SIGNAL

	Intramuscular		Epicardial		
	Needle		Disc	Catheter	
US frequency (MHz)	1.0	0.5	0.5	0.5	1.0
Peak pressure (MPa)	3.4	0.7	0.7	0.7	3.4
US intensity (W/cm^2)	0.85	0.18	0.18	0.18	0.85
Axial resolution (mm)	1.6	3.1	3.1	3.1	1.6
Lateral resolution (mm)	2.5	4.2	4.2	4.2	2.5
AE (pk, μV)	1.40	2.09	0.52	1.70	1.14
AE/Pressure (μV/MPa)	0.42	2.99	0.74	2.43	0.34
ECG (pk, mV)	16.6	9.4	3.4	11.9	9.6
AE/ECG ($\times 10^{-3}$)	0.08	0.22	0.15	0.14	0.12
Noise (RMS, μV)	0.10	0.10	0.07	0.10	0.11
SNR (dB)	22.9	26.4	17.4	24.6	20.3

using the same experimental setup and rabbit heart. The peak AE amplitudes were 1.67 and 1.14 μV for the 0.5- and 1.0-MHz transducers, respectively. When normalized by the ultrasound pressure, the peak AE amplitudes were 2.39 μV/MPa (at 0.5 MHz) and 0.34 μV/MPa (at 1.0 MHz) or a ratio of 7.0.

Performance results for each experiment and recording scenario are summarized in Table I.

C. Cardiac Activation Mapping Using UCSDI and the Clinical Cardiac Catheter

Results suggest that UCSDI provides additional spatial and temporal information for mapping the cardiac activation wave. As described in background and theory, the ECG_{LF} does not have the same temporal profile as the ECG_{AE} signal, which depends on the location of the ultrasound beam in the heart. To explore this further in the live rabbit heart and map cardiac activation with UCSDI, we scanned the ultrasound transducer to produce B-mode (2-D) and volume (3-D) images during the cardiac cycle using a setup similar to Fig. 5(a). The total scan length for B-mode imaging was 14 mm with 1-mm steps. The white arrow in Fig. 6(a) indicates the scan region and direction. A superimposed B-mode pulse-echo image (grayscale) and UCSDI image (hot colors) are displayed in Fig. 6(b). The pulse echo image clearly displays the RV and LV walls of the heart along with the hypoechoic interior of the ventricles. The largest AE signals were observed near recording electrode R_2 due to the strong lead field at this location.

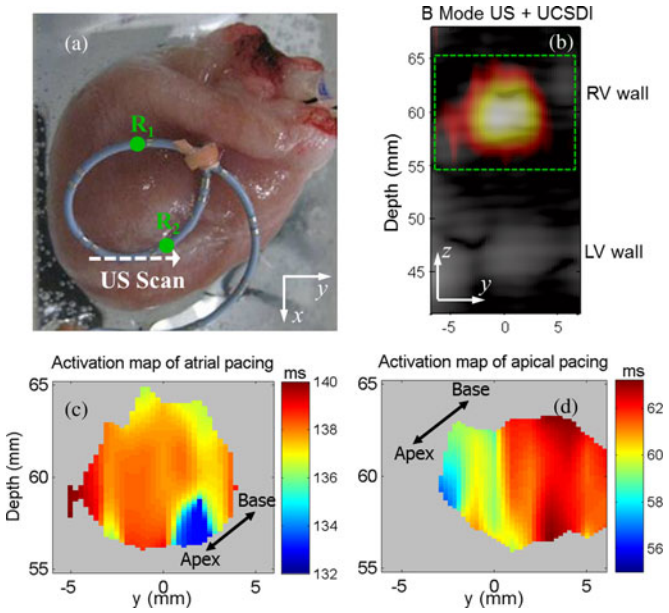

Fig. 6. (a) Top view (*xy* plane) of the rabbit heart, recording electrodes, and B-mode scanning range and direction. The scan size is 14 mm with 1 mm steps. Each image represents an average of 50 consecutive cardiac cycles at each scan point. (b) Superposition of the pulse echo B-mode image (grayscale) and UCSDI (hot colors) in *yz* plane. Pulse echo images are generated from the echo of the ultrasound pulse, while the UCSDI maps are produced from the AE signal at the peak envelope of the ECG_{LF} ($t = 139$ ms). The vertical axis (depth) is the same as for the M-mode images. The horizontal axis represents the lateral scan position in millimeters. The images are interpolated and displayed on a dB scale (35 dB for pulse echo and 10 dB for UCSDI). (c) Activation map inside the dashed green box from (b) with stimulation at the SA node. Colors denote the arrival time (in ms) of the peak envelope of the ECG_{AE} signal at each position. Gray pixels represent ECG_{AE} signals below a threshold of 40% of the maximum AE signal. (d) Activation map for a second scan with stimulation near the apex.

In addition to measuring the spatial pattern of the ECG, we also examined current propagation over time as a possible method to track reentry loops or other conduction abnormalities. Activation times were determined from the delay between the pacing pulse and the peak of the ECG_{AE} envelope at each pixel, producing a 2-D activation map from a B-mode UCSDI dataset. Fig. 6(c) displays the cardiac activation map over the region of interest depicted in Fig. 6(b). Red indicates the arrival of the ECG occurred later. From this map, we can clearly visualize cardiac activation from base to apex, a pattern consistent with atrial pacing.

The activation map indicates that the local activation time varied from 132 to 140 ms in the scan region (137.5$\pm$1.3 ms). However, the distribution of activation times based on the standard ECG_{LF} was much narrower, ranging from 135.9 to 136.9 ms (136.4$\pm$0.3 ms). The variability of activation times based on the ECG_{LF} was less than for the ECG_{AE}. This was expected because only the ECG_{AE} signal depends on the location of the

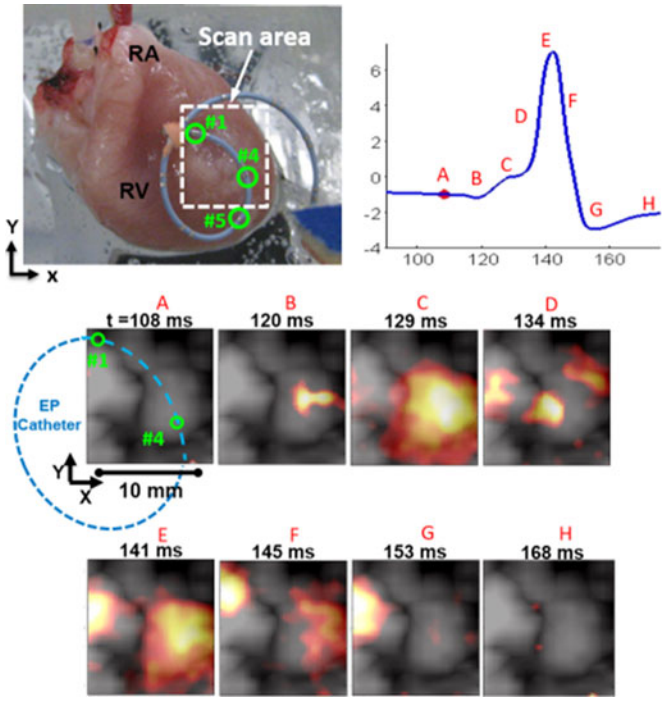

Fig. 7. Volume activation maps produced by an XY scan of the ultrasound beam. (Upper left) Rabbit heart, catheter position, recording electrodes, and scan area. (Upper right) $\mathrm{ECG_{LF}}$ signal [ms, mV]; (bottom) UCSDI images (color) superimposed with pulse-echo images (gray) during the cardiac cycle. The UCSDI image are generated from the maximum intensity projection of the AE signal in the z (depth) direction. These data are part of a 4-D (volume + time) pattern that are presented as a UCSDI movie (UCSDI_AE_PE_MIP_XY.avi). The UCSDI maps reveal the magnitude of the current density at different locations and times.

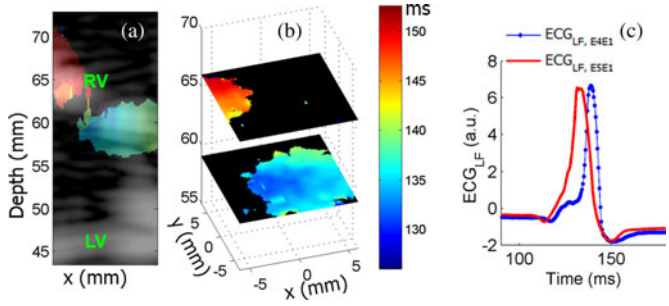

Fig. 8. (a) Superposition of pulse echo (gray) B-mode image and cardiac activation map (color) at y = 1 mm position; Images at different x and y positions can be viewed in the movie UCSDI_ActvMap_with_PE_3D.avi. (b) Two horizontal slices of the 3-D activation map at a depth of 59 and 66 mm. (c) $\mathrm{ECG_{LF}}$ signals from two pairs of electrodes. The electrodes were marked in Fig. 7 as #1, #4, and #5. The blue dotted curve is the $\mathrm{ECG_{LF}}$ signal measured using electrodes #4 and #1 in differential mode; the red solid curve is the $\mathrm{ECG_{LF}}$ signal measured using electrodes #5 and #1.

ultrasound beam in the heart. Therefore, the range of activation times of the $\mathrm{ECG_{AE}}$ during the scan were expected to have a larger variation than the fixed $\mathrm{ECG_{LF}}$ signal. This result illustrates that the spatial and temporal pattern of the ECG can be obtained by scanning an ultrasound beam to different locations heart, while recording the AE interaction signal on a single pair of electrodes.

Fig. 6(d) presents a second activation map from the same heart as Fig. 6(c) but with *apical* pacing, which should activate the myocardium from apex to base. The average peak time of the $\mathrm{ECG_{AE}}$ signals was 59 ms, which occurred much earlier than that for atrial pacing (132 ms). This was expected because apical pacing bypassed the normal delay through the atrioventricular node. The average conduction velocity for apical pacing was 0.67 ± 0.06 m/s compared to 1.31 ± 0.20 m/s for atrial pacing.

In addition to B-mode UCSDI, we also performed a C-scan along the *x*- and *y*-axes to produce 3-D activation maps during RA pacing. The scan area was 13 mm (*x*) by 15 mm (*y*). A sequence of UCSDI images (*xy* lateral planes) during the cardiac cycle (A-H) at the RV wall are illustrated in Fig. 7. These maps reveal the cardiac activation pattern captured by UCSDI using the $\mathrm{ECG_{LF}}$ as a reference. The strongest AE signals were observed from time point "C" to "G," which was consistent with the strongest activation times of the $\mathrm{ECG_{LF}}$.

Based on the data described in Fig. 7, 3-D activation maps were generated and displayed in Fig. 8. The vertical cross section of the activation map superimposed with the pulse echo image [see Fig. 8(a)] confirmed that the detected activation region was located at the RV wall. The red and blue regions correspond to regions near recording electrodes #1 and #4, respectively. Lateral (*XY*) slices at different depths [see Fig. 8(b)] help visualize the 3-D cardiac activation. These images indicate that the AE signal near electrode #4 occurred earlier than the region near electrode #1.

To verify this activation pattern, we used the simultaneously recorded $\mathrm{ECG_{LF}}$ signal from another pair of electrodes (#5 and #1 marked in Fig. 7), denoted as $\mathrm{ECG_{LF,E5E1}}$. The latency of the two $\mathrm{ECG_{LF}}$ signals is compared in Fig. 8(c). The earlier arrival of the $\mathrm{ECG_{LF}}$ from electrode #5 is consistent with the activation pattern displayed in Fig. 8(a) and (b).

IV. Discussion

This study compared different ultrasound frequencies and electrode configurations for mapping the live rabbit heart with UCSDI. According to Table I, intramuscular recording at 0.5 MHz produced the best sensitivity for detecting the AE signal (3.0 μV/MPa). This was likely due to invasive electrodes placed directly in the myocardium and their strong lead fields directly in the path of the cardiac current flow. The unshielded and flexible disc array, on the other hand, exhibited the poorest sensitivity (0.74 μV/MPa). The difficulty maintaining firm contact with the epicardium may have contributed to lower sensitivity and higher background noise. This was further supported by the weaker $\mathrm{ECG_{LF}}$ signal captured by the disc electrodes. Meanwhile, the shielded catheter electrodes placed on the epicardium provided an excellent balance between invasiveness (surface recording) and detection sensitivity (2.4 μV/MPa).

We also examined the effect of the ultrasound frequency on the sensitivity and resolution of UCSDI. The sensitivity at 0.5 MHz was seven times larger than that at 1 MHz (3.0 μV/MPa versus 0.41 μV/MPa). This is likely due to the greater integration volume at the focal zone of the 0.5-MHz transducer (approximately eight times as a first-order approximation). On the other hand, the 1-MHz transducer demonstrated a better spatial resolution than the 0.5-MHz transducer indicated by the smaller

axial spot size of the current densities in the RV wall (3.19 versus 6.21 mm). This further illustrates the tradeoff between spatial resolution and sensitivity for UCSDI.

The recording electrode lead field is also a key factor that affects the amplitude of the AE signal. This has been more thoroughly explored in our previous work [13], [16], [17]. In general, to optimize detection of the AE signal, the recording electrodes should be configured so that the lead field is parallel to the propagation of electrical current. However, the cardiac activation time (or activation map) is largely unaffected by the orientation of the lead field as long as there is sufficient sensitivity to detect the AE signal. The dependence of UCSDI on the lead field can be reduced or eliminated by recording with multiple leads (i.e., more than two electrodes).

Fig. 6(b) displayed a current density image at the peak of the $\mathrm{ECG_{LF}}$ superimposed on the B-mode pulse echo image, highlighting the LV and RV walls of the heart. The integration of UCSDI with standard echocardiography is a potentially powerful combination for EAM during treatment of arrhythmias. Based on the same dataset, activation maps were generated from atrial and apical pacing and a single pair of differential recording electrodes. Overall, the latencies of the peak $\mathrm{ECG_{AE}}$ were highly correlated with those of the $\mathrm{ECG_{LF}}$. However, the $\mathrm{ECG_{AE}}$ exhibited a higher variability of latencies due to the sampling at different locations in the heart by scanning the ultrasound beam. The spatial information provided by UCSDI revealed current propagation from base to apex with atrial pacing, and propagation in the reverse direction with apical pacing, as well as a shorter average latency (59 versus 132 ms). The maps [see Fig. 6(c) and (d)] further indicated slight variations of the ECG activation times between the epicardium and the endocardium, consistent with another isolated rabbit heart study [18]. Normally, EP information related to transmural propagation would have required separate contact electrodes placed on the epicardium and endocardium, but UCSDI was able to capture depth information as the ultrasound pulse passed from the RV endocardium to the epicardium.

This study has demonstrated that UCSDI in principle can effectively localize the ECG signal and map the cardiac activation wave. While real-time M-mode imaging was possible with the described system, B-mode and volume imaging depended on slow mechanical scanning of the US xducer. A 2-D B-mode image including 50 averages of the cardiac cycle required less than 5 min. The acquisition time could be dramatically improved using *electronic* scanning of the ultrasound beam, similar to what is used in standard echocardiography. Also, because the ECG precedes the mechanical contraction, cardiac motion is less of a concern for UCSDI. This study also employed the electromechanical decoupler BDM to help reduce cardiac motion and maintain the same reference frame over multiple cardiac cycles, which was important for 2-D and 3-D imaging.

V. Conclusion

This study provided a baseline for detecting the AE signal in the rabbit heart using different recording configurations and ultrasound frequencies. Two-dimensional and volume mapping of the cardiac activation wave were also demonstrated using UCSDI with a clinical cardiac catheter. Finally, coregistered pulse echo ultrasound images helped identify the LV and RV walls, providing an important anatomical reference for the current density maps. Intracardiac echocardiography combined with real-time UCSDI holds great promise for rapid and accurate cardiac mapping prior to ablation therapy for sustained and unsustained arrhythmias.

References

[1] S. W. Huang, "Preface," in *Radiofrequency Catheter Ablation of Cardiac Arrhythmias: Basic Concepts and Clinical Applications*, S. K. S. Huang and D. J. Wilber, Eds., Armonk, NY, USA: Futura Publishing Company, Inc., 2000.

[2] M. Schmidt, U. Dorwarth, D. Andresen, J. Brachmann, K. H. Kuck, M. Kuniss, T. Lewalter, S. Spitzer, S. Willems, J. Senges, C. Jnger, and E. Hoffmann, "Cryoballoon versus RF ablation in paroxysmal atrial fibrillation: Results from the German ablation registry," *J. Cardiovasc. Electrophysiol.*, vol. 52, no. 1, pp. 1–7, 2013.

[3] A. Gupta and A. Maheshwari, "Cardiac mapping: Utility or futility," *Indian Pacing Electrophysiol. J.*, vol. 2, no. 1, pp. 20–32, 2002.

[4] D. Bhakta and J. M. Miller, "Principles of electroanatomic mapping," *Indian Pacing Electrophysiol. J.*, vol. 8 no. 1, pp. 32–50, 2008.

[5] R. Witte, R. Olafsson, S.-W. Huang, and M. O'Donnell, "Imaging current flow in lobster nerve cord using the acoustoelectric effect," *Appl. Phys. Lett.*, vol. 90, pp. 163902-1–163902-3, 2007.

[6] Q. Li, R. Olafsson, P. Ingram, Z. Wang, and R. Witte, "Measuring the acoustoelectric interaction constant using ultrasound current source density imaging," *Phys. Med. Biol.*, vol. 57, no. 19, pp. 5929–5941, 2012.

[7] F. Fox, K. Herzfeld, and G. Rock, "The effect of ultrasonic waves on the conductivity of salt solutions," *Phys. Rev.*, vol. 70, pp. 329–339, 1946.

[8] J. Jossinet, B. Lavandier, and D. Cathignol, "The phenomenology of acousto-electric interaction signal in aqueous solutions of electrolytes," *Ultrasonics*, vol. 36, pp. 607–613, 1998.

[9] J. Jossinet, B. Lavandier, and D. Cathignol, "Impedance modulation by pulsed ultrasound," *Ann. N.Y. Acad. Sci.*, vol. 873, pp. 396–407, 1999.

[10] B. Lavandier, J. Jossinet, and D. Cathignol, "Quantitative assessment of ultrasound-induced resistance change in saline solution," *Med. Biol. Eng. Comput.*, vol. 38, no. 2, pp. 150–155, 2000.

[11] B. Lavandier, J. Jossinet, and D. Cathignol, "Experimental measurement of the acousto-electric interaction signal in saline solution," *Ultrasonics*, vol. 38, no. 9, pp. 929–936, 2000.

[12] H. Zhang and L. Wang, "Acousto-electric tomography," *Proc. SPIE*, vol. 5320, pp. 145–149, 2004.

[13] R. Olafsson, R. Witte, S.-W. Huang, and M. O'Donnell, "Ultrasound current source density imaging," *IEEE Trans. Biomed. Eng.*, vol. 55, no. 7, pp. 1840–1848, Jul. 2008.

[14] R. Olafsson, R. Witte, C. Jia, S.-W. Huang, K. Kang, and M. O'Donnell, "Cardiac activation mapping using ultrasound current source density imaging (UCSDI)," *IEEE Trans. Ultrason. Ferroelectr. Freq. Control*, vol. 56, no. 3, pp. 565–574, Mar. 2009.

[15] Y. Qin, Z. Wang, P. Ingram, Q. Li, and R. S. Witte, "Optimizing frequency and pulse shape for ultrasound current source density imaging," *IEEE Trans. Ultrason. Ferroelectr. Freq. Control*, vol. 59 no. 10, pp. 2149–2155, Oct. 2012.

[16] Z. Wang, R. Olafsson, P. Ingram, Q. Li, Y. Qin, and R. S. Witte, "Four-dimensional ultrasound current source density imaging of a dipole field," *Appl. Phys. Lett.*, vol. 99, no. 11, pp. 113701–1137013, 2011.

[17] Z. Wang and R. S. Witte, "Simulation-based validation for four-dimensional multi-channel ultrasound current source density imaging," *IEEE Trans. Ultrason. Ferroelectr. Freq. Control*, vol. 61 no. 3, pp. 420–427, Mar. 2014.

[18] R. Wolk, K. A. Kane, S. M. Cobbe, M. N. Hicks, "Regional electrophysiological effects of hypokalaemia, hypomagnesaemia and hyponatraemia in isolated rabbit hearts in normal and ischaemic conditions," *Cardiovasc. Res.*, vol. 40, no. 3, pp. 492–501, 1998.

Authors' photographs and biographies not available at the time of publication.